Structural determination of Bi-doped magnetite multifunctional nanoparticles for contrast imaging†

M. A. Laguna-Marco,[*a] **C. Piquer,**[a] **A. G. Roca,**[b] **R. Boada,**[c] **M. Andrés-Vergés,**[d] **S. Veintemillas-Verdaguer,**[e] **C. J. Serna,**[e] **A. Iadecola,**[f] **and J. Chaboy** [a]

To determine with precision how Bi atoms are distributed in Bi-doped iron oxide nanoparticles their structural characterization has been carried out by X-ray absorption spectroscopy (XAS) recorded at the K edge of Fe and at the L_3 edge of Bi. The inorganic nanoparticles are nominally hybrid structures integrating an iron oxide core and a bismuth oxide shell. The XAS spectra show that, in the samples synthesized by precipitation in aqueous media and laser pyrolysis, the Bi atoms neither enter in the iron oxide spinel lattice nor form any other mixed Bi-Fe oxide. No modification of the local structure around the Fe atoms induced by the Bi atoms is observed at the Fe K edge. In addition, contrary to expectations, our results indicate that the Bi atoms do not form a well defined Bi oxide structure. The XAS study at the Bi L_3 edge indicates that the environment around Bi atoms is highly disordered and only a first oxygen coordination shell is observed. Isolated $[BiO_{6-x}(OH)_x]$ units (or similar) bonded through hydroxyl bridges to the nanoparticle, rather than a well defined Bi_2O_3 shell, are surrounding the nanoparticle. On the other hand, the XAS study indicates that, in the samples synthesized by thermal decomposition, the Bi atoms are embedded in a longer-range ordered structure showing first and second neighbors.

1 Introduction

Multifunctional nanoparticles combining magnetic and optical properties in a single entity have been recently proposed as new-generation contrast and therapeutic agents in biomedicine [1,2]. To date, superparamagnetic iron oxide nanoparticles have been seen as the most promising materials for many medical applications due to their magnetic properties, chemical stability, biocompatibility and low price. [3–5] Together with Gd chelates, superparamagnetic iron oxide nanoparticles are the most used contrast agents for the detection of tumors by Magnetic Resonance Imaging (MRI) [3,6]. However, in some cases, imaging results are too vague to provide detailed enough bio-logical information [7]. To further improve the sensitivity and efficiency in imaging techniques many efforts focus nowadays on synthesizing hybrid nanostructures where each of the components of the heterostructure is aimed at an specific task. Thus, magneto-luminiscent nanoparticles have been proposed for diagnosis imaging, but this class of materials present serious drawbacks related with the luminescent properties [8]. Alternatively, multifunctional particles combining good magnetic response and high X-ray absorption coefficient, for instance including a heavy element such as bismuth, emerge as a promising tool in the field [9]. These particles are able to be imaged by both MRI and Computed Tomography (CT) providing higher sensitivity. This approach, however, has not been explored much yet, even when Bi has a long bioutility history and CT is one of the most common imaging techniques [10–13].

Recent works on Bi-doped nanoparticles have suggested that the Bi atoms do not enter the spinel lattice, but form a core/shell magnetite/bismuth oxide heterostructure [14]. According to these results, Bi acts as surfactant controlling particle size and colloidal properties. Although the formation of a bismuth oxide phase was proposed, no detailed structural study of this Bi phase has been performed yet in this type of nanoparticles. The location and type of bonds of Bi determine to a high extent the size, shape and physicochemical properties (stability or degradation in biological media, partial release or toxicity) of the nanoparticles and so their functionalization and application as double contrast agents for imaging. Therefore

an accurate determination of the environment around Bi is of paramount importance.

To provide a microstructural determination of how the bismuth atoms enter these systems we present here a detailed X-ray Absorption Spectroscopy (XAS) study on several Bi-doped iron oxide nanoparticles with sizes below the monodomain diameter (6-30 nm range), different amount of Bi doping and synthesized by up to three different routes. Both energy regions of the XAS spectra, i.e. X-ray Absorption Near Edge Structure (XANES) and Extended X-ray Absorption Fine Structure (EXAFS), have been recorded at the K edge of iron and and L_3 edge of bismuth. The analysis of the modulations in the X-ray absorption coefficient recorded at both regions provide complementary information about the local structure around the absorbing atoms: distances to, number and nature of neighboring atoms as well as type of coordination (geometry) around the absorbing atoms. XAS is an atomic specific experimental probe that does not require any long range crystal symmetry and hence permits us to have direct access to the local atomic structure of a wide variety of materials, including amorphous materials, liquids and nanoparticles. The study of the XAS recorded at the Fe K edge will let us know the environment around Fe atoms and whether the nanoparticles fully correspond to the nominal Fe_3O_4 magnetite or not. The Bi L_3-edge absorption spectrum will provide the accurate determination of the local environment around Bi.

For the analysis of the signals recorded at the Fe edge, we have compared both XANES and EXAFS signals to a number of references. In addition, by using the Fourier transform of the EXAFS signal (FT, which roughly speaking gives us the atomic radial distribution function in R-space) the evolution of the environment around Fe with the amount of Bi doping has been studied. To this aim, the experimental data have been compared to theoretical FEFF calculations. Regarding the spectra recorded at the Bi L_3 edge, as a first step we have compared the signals of the nanoparticles to a number of reference compounds. Further analysis of the atomic distribution around the Bi atom has been carried out by comparing the experimental signals (including Fourier transforms and Fourier back-transforms i.e. Fourier filtered n-shell EXAFS oscillations), to *ab-initio* computations.

2 Experimental and computational methods

Fe oxide nanoparticles containing different amounts of bismuth were synthesized following three different routes: laser pyrolysis (LP), precipitation in aqueous media (PAM) and thermal decomposition (TD). In all the synthesis we tried to dope iron oxide nanoparticles with less than 10 % in bismuth to reach similar sizes than the ones published before [14,15]

Samples PAM1, PAM2 and PAM7 were synthesized by precipitating iron(II) and bismuth(III) nitrate in a mixture of al-

kaline media and ethanol. The reaction was carried out in a three-necked 500 cm^3 round-bottom flask placed in an oil bath with mechanical stirring using a dual glass blade and under nitrogen flow. In a typical experiment, a mixture of iron and bismuth salts (different molar Fe/Bi ratios) in 20 mL of water 0.02 M H_2SO_4, 0.07 M NaOH and 0.1 M KNO_3 (180 mL water/ethanol 80:100), were degasified for 1 h by nitrogen bubbling and mixed at room temperature. When the precipitation was completed, the system was heated to 90 °C and left undisturbed for 24 h. Then the suspension was cooled at room temperature with an ice bath, and the solid was separated by magnetic decantation and washed several times with distilled water. [15]

Sample LP10 was obtained by the decomposition of iron pentacarbonyl ($Fe(CO)_5$, 30 °C) and bismuth triethyl (TBI, -7.5 ° C) after heating a mixture of argon and air with ethylene under the action of a continuous-wave carbon dioxide laser ($\lambda = 10.60 \pm 0.05$ μm, energy density= 652 Wcm^{-2}). [16,17] Above a certain pressure and laser power, a critical concentration of product nuclei is formed in the reaction zone. This leads to homogeneous nucleation of particles that are carried to a filter by an inert gas. Other constant parameters of the experiment were: laser power, 82 W; argon axial flux, 15 sccm; argon windows flux, 220 sccm; pressure, 400 mbar; reactive temperature, 20 °C; TBI carrier gas was N_2 4sccm; $Fe(CO)_5$ carrier gas was a mixture of air 3.1 sccm and ethylene 7 sccm; average duration of the experiment, 5 h.

Sample TD03 consists on bismuth doped nanoparticles obtained by thermal decomposition of $Fe(acac)_3$ and $Bi(acet)_3$ in the presence of oleic acid and oleylamine as surfactants, and benzyl ether. [18] A mixture of 5.03 g $Fe(acac)_3$ (14.25 mmol), 0.290 g $Bi(acet)_3$ (0.75 mmol), 16.93 g 1,2-dodecanediol (75 mmol), 14.19 g oleic acid (45 mmol), 17.27 g oleylamine (45 mmol), and 150 mL benzyl ether was put into a four-necked flask and heated up to 200 °C for 120 min with magnetically stirring and under a nitrogen flow. Then, the solution was heated to reflux (b.p. $\sim$ 300 °C) for 30 min in a N_2 atmosphere. To remove impurities, the solution at room temperature was mixed with ethanol, centrifuged at 5650g for 10 min and the supernatant discarded. Finally, nanoparticles were mixed with 40 ml of hexane and 0.1 ml of oleic acid, and centrifuged twice at 5650g for 10 min. Powders from these suspensions were obtained by precipitation with ethanol and dryness at room temperature under a N_2 flow.

Morphology, particle size, and distribution were investigated using a transmission electron microscope (JEOL-2000 FXII) operating at 200 keV. HRTEM images were obtained by means of a Philips TECNAI 200 T. Mean size (D) and the standard deviation (SD) associated with it were evaluated from the electron micrographs by counting around 500 particles. The microstructure of the obtained nanoparticles was analyzed by powder X-ray diffraction (XRD) at room temperature, using

a rotating-anode Rigaku diffractometer in the Bragg-Brentano geometry, with Cu-Kα radiation. The crystallite size was determined from the full-width at half-maximum of the reflection (311) of magnetite by using the Scherrer equation. Iron and bismuth content in the magnetite samples was determined by plasma emission (ICP, PERKIN ELMER OPTIMA 2100 DV). For this analysis, 25 mg of powder were first dissolved with concentrated HCl and then diluted with doubly distilled water.

Fe K-edge and Bi L_3-edge XAS spectra were recorded at the bending magnet XAFS beamline of the ELETTRA Synchrotron Facility (Trieste, Italy) [19]. Experiments were performed at room temperature and in the transmission mode using three ionization chambers mounted in series for simultaneous measurements on the sample and a reference. Fe and Bi foils were used as reference for calibration checking purposes. Measurements were also performed in the fluorescence mode by using a single-element Si-drift detector (SDD). No difference, other than a lower signal to noise ratio, was found with respect to the transmission ones. The energy of the incoming X-ray beam was tuned with a Si(111) double-crystal monochromator to probe the absorption at the Fe K edge and the Bi L_3 edge. Harmonic rejection was achieved by detuning the second crystal from parallel alignment at Fe K-edge energy.

Standard $\sim$ 13 mm-diameter pellets of the powdered samples thoroughly mixed with boron nitride were made. Total thickness of the samples was in the 300-700 μm range to assure they could be handled without breaking. The amount of sample was optimized to obtain the best signal-to-noise ratio ($\sim$ 0.7 edge jump height at the Fe K edge).

A number of reference samples have also been measured: bulk Fe_3O_4 (magnetite), γ-Fe_2O_3 (maghemite), α-Fe_2O_3 (hematite), FeO(OH) (goethite) and FeO (wustite) at the Fe K edge and Bi metal, $BiFeO_3$, α-Bi_2O_3, β-Bi_2O_3, $Bi(OH)_3$ and the precursors $Bi(acet)_2$ and $Bi(NO_3)_3$ at the Bi L_3 edge.

The EXAFS spectra were analyzed according to standard procedures [20] using the HORAE-IFEFFIT (Athena, Artemis) program package and the FEFF code for the *ab-initio* multiple scattering EXAFS simulations. [21,22] The ab-initio computation of the XANES spectra was carried out using the multiple-scattering code Continuum [23] included in the MXAN package [24]. For the computations the potential for the different atomic clusters was approximated by a set of spherically averaged muffin-tin (MT) potentials built by following the standard Mattheis' prescription. The muffin-tin radii were determined following the Norman's criterion. For the reference compounds we have first determined the minimum size of the cluster needed to reproduce all the features of the experimental XANES spectrum. This is made by adding progressively coordination shells surrounding the absorbing atom until convergence is obtained, i.e. the addition of further shells do not

lead to the modification of the relative energy separation and intensity of the spectral features or to the appearance of new ones. Then, care was taken to determine the best choice for the overlapping factor (ovf) between the muffin-tin spheres and for the exchange and correlation components of the final state potential. [25–27] Thus, in a second step we have checked the influence of the ovf used to built up the scattering potential into the reproduction of the experimental XANES spectra. Moreover, we have also studied the effect of modifying the value of the maximum angular momentum quantum number, l_{max}, needed to account for the experimental absorption spectrum in the first $\sim$ 50 eVs. Last but not least we have studied the best choice of the exchange and correlation part of the final state potential (ECP) to reproduce not only the spectral shape but also the intensity of the computed spectral features and their relative energy separation. To this end we have performed the computations by using (i) the energy dependent Hedin-Lundqvist (HL) ECP potential, (ii) the energy dependent Dirac-Hara (DH) ECP potential, (iii) only the real part of the HL ECP (hereafter *real* HL) and (iv) by adding the imaginary part of the HL ECP to the Dirac-Hara one (hereafter *complex* Dirac-Hara). The best reproduction of the experimental XANES spectra was obtained by using the Dirac-Hara ECP potential and by imposing a 1% of overlapping factor, in agreement to previous works for transition metal oxides and related compounds [27–29]. In order to get an enhanced view of the differences the results obtained in the case of using the real DH ECP are shown. A complete discussion of the procedure can be found elsewhere [30–32]. The theoretically calculated spectra have been directly compared to the experimental XANES spectrum i.e., no fitting procedure (free parameter) has been used during the calculations. The assessment of the quality of the theoretical computations is based on the correct reproduction of the shape and energy position of the different spectral features and of their relative energy separation and the intensity ratio. For the rest of the computations we have just determined the minimum size of the cluster needed to reproduce all the features of the experimental XANES spectrum. The overlapping factor and the exchange and correlation components of the final state potential have been fixed to those found for the reference compound. In all the cases, the theoretical spectra have been convoluted with a Lorentzian shape function (Γ = 1.5 eV for Fe K edge, 5.98 eV for Bi L_3 edge) to account for the core-hole lifetime [33] and the experimental resolution.

3 Results and discussion

3.1 TEM and XRD Structural Characterization

The studied samples, synthesized by the different methods described above, are listed in table 1. The Bi content, parti-
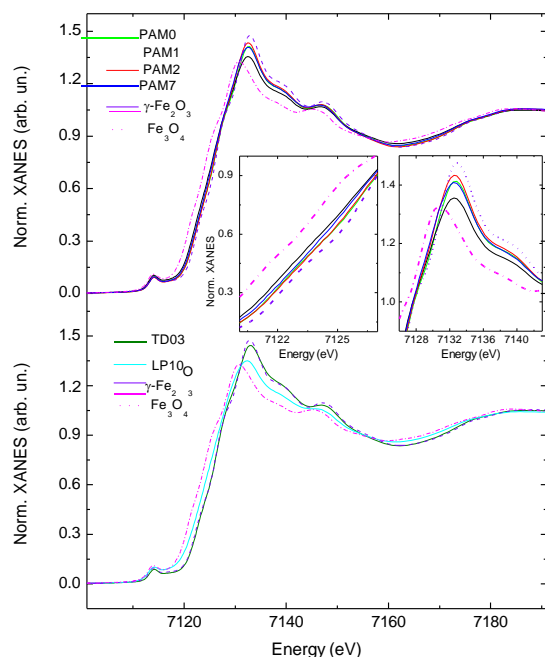
Fig. 1 (Experimental Fe K-edge XANES spectra of bismuth-doped iron oxide nanoparticles and reference samples. Insets: zoomed threshold (left) and white line (right) regions .

cle size measured by TEM and crystallite size calculated from Scherrer's equation (D_{XRD}) are also summarized in the table.

Representative TEM images of the nanoparticles synthesized by the three methods and the X-ray diffractograms of all the samples are reported in the supplementary information. XRD patterns of all the samples show a main phase that corresponds to iron oxide with an inverse spinel structure, either magnetite or maghemite.

3.2 Fe K-edge XANES and EXAFS Characterization

The Fe K-edge XANES spectra of all the measured Bi-doped iron oxide nanoparticles are shown in Fig. 1. The spectra corresponding to bulk Fe_3O_4 (magnetite) and γ-Fe_2O_3 (maghemite) references are also included. All the Bi-doped samples present an absorption profile that lies in between those of maghemite and magnetite references. The presence of precursors as well as the formation of other Fe oxides or hydroxides can be discarded by simple comparison of the spectral shapes (see supplementary information). Further confirmation has been obtained by fitting the spectra of the nanoparticles to the weighted addition of reference spectra following the procedure previously used by Piquer et. al. [34] This procedure gives no appreciable amount of these references for the best fits (not shown).

No crystallographic change due to the Bi atoms entering in the iron-oxide nanoparticles can be observed. It should be noted that in the case of the native oxides the average Fe-O interatomic distance is $\sim$ 1.98 Å while the nominal average Bi-O distance is $\sim$ 2.50 Å for both α- and β-Bi_2O_3. Consequently, if Bi entered the iron oxide by substituting Fe, there would be an structural distortion, through the modification of the Fe(Bi)-O and Fe(Bi)-O-Fe(Bi) interatomic distances, that should be reflected in the absorption spectra. In the case of XANES the modification of these distances should imply both the marked shift of the edge position as well as changes in the overall spectral shape [31,35–37]. None of these modifications has been detected. Similarly, changes are expected in the EXAFS part of the spectra if Bi substitutes Fe, but, as in the XANES case, these effects have not been observed. In particular, comparing the EXAFS spectra of the PAM series (see top panel of Fig. 2) no shift is observed in any of the spectral features, indicating no changes in the cell parameters and/or interatomic distances. Similarly, the amplitude of the EXAFS oscillations does not show any gradual evolution as the Bi content is increased. The lack of a Bi effect on the Fe K-edge spectra can be clearly seen when comparing the FT of the EXAFS signal corresponding to the experimental data and the FEFF simulations (middle and bottom panels of Fig. 2, respectively). According to the FEFF simulations, the Bi substitution should give rise to a gradual intensity decrease of both first and second peak as the Fe atoms are replaced by Bi in a 0, 2 or 7%. (See the supplementary information for the details about the EXAFS analysis and theoretical calculations.) The experimental data, however, show a random evolution with Bi content. Therefore, the differences observed between the spectra of the PAM series cannot be explained in terms of the presence of substitutional Bi in the iron oxide matrix. In the same way, if the bismuth atoms entered interstitially in the lattice a strong structural distortion and a concomitant gradual change in the profile of the XAS (both XANES and EXAFS) spectra should be expected, contrary to the observed behavior. On the other hand, the observed differences can be related to the formation of non-stoichiometric Fe oxides ($Fe_{3-\delta}O_4$) due to the size reduction. The size reduction makes it very difficult to obtain nanoparticles that are perfect magnetite or maghemite, i.e. with exactly the same structural parameters and oxidation state as in the bulk compound. Indeed, differences like these ones are typically observed in iron oxide nanoparticles with no doping included. [34] The crystallographic particularities of each non-stoichiometric oxide (i.e. number and type of vacancies, oxidation states, exact values of the lattice parameters, etc) depend on the details of the growth process undergone in each sample and will affect the profile of the XANES and EXAFS (and their FT). [34]

No modification of the local structure around the Fe atoms induced by the Bi atoms is observed at the Fe K edge. Truly,

Table 1 Studied samples, preparation route, bismuth concentration determined by plasma emission (given in Bi/Fe atomic ratio, $(Bi/Fe)_{at} \times 100$), particle size measured by TEM (nm) and crystallite size calculated from XRD data (nm).

Sample	Preparation method	Bi %	TEM size (nm)	XRD size (nm)
PAM1	Precipitation in aqueous media	1	30 ± 5	27 ± 1
PAM2	Precipitation in aqueous media	2	27 ± 5	21 ± 1
PAM7	Precipitation in aqueous media	7	20 ± 4	13 ± 1
LP10	Laser pyrolysis	10	12 ± 4	5 ± 1
TD03	Thermal decomposition	0.3	6 ± 2	6 ± 1
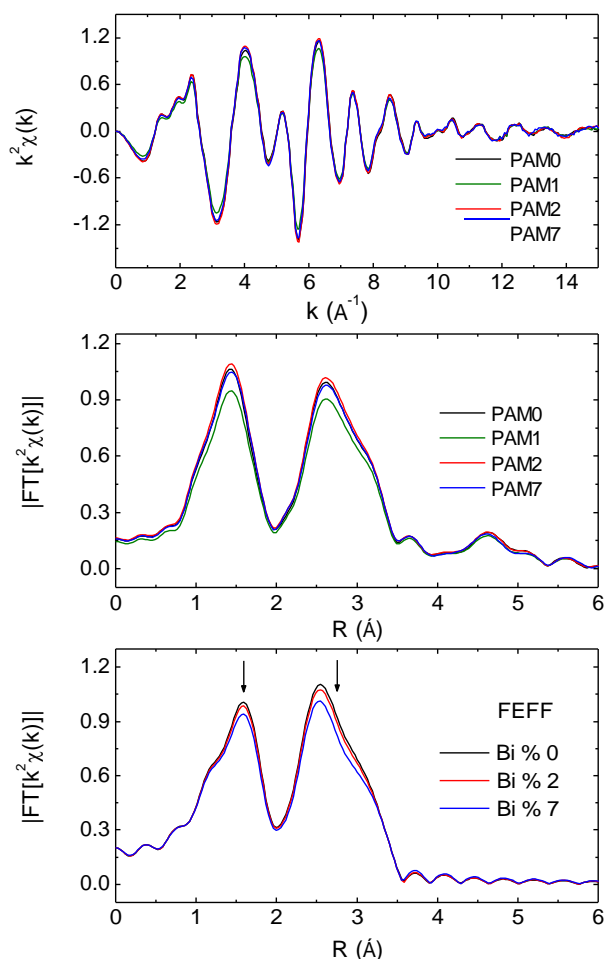
Fig. 2 (top) Comparison of the experimental Fe K-edge EXAFS spectra of the nanoparticles synthesized by precipitation in aqueous media with different Bi content: 0, 1, 2 and 7 %. (middle) modulus of the Fourier transform obtained from the experimental EXAFS signals. (bottom) FEFF calculated modulus of the Fourier transform for different Bi content: 0, 2 and 7% substitutional Bi in the Fe_3O_4 crystal structure.

an scenario where the effects of bismuth on the Fe signal are hindered in the averaged response of all the Fe atoms cannot be ruled out. In addition, it cannot be completely discarded that only a smaller part of the Bi atoms are located inside the nanoparticle. Nevertheless, the comparison in Fig. 2 suggests that the Bi atoms neither enter in the spinel structure substituting Fe nor in interstitial sites. Moreover, the structural environment of the Fe atoms remain unaltered and highly ordered. These conclusions are sustained on the analysis of both XANES and EXAFS regions of the spectra coupled with theoretical simulations. Since the bismuth atoms, are not located within the iron oxide lattice, they are expected to be in another phase around the iron oxide grain.

3.3 Bi L_3-edge XANES - PAM and LP samples

The Bi L_3-edge XANES spectra of the samples are shown in Fig. 3 (a). As in the Fe K edge case, all the spectra corresponding to the samples under study are very similar (with the exception of TD03, which deserves special attention). A simple fingerprint analysis discards the presence of Bi-containing precursors, as well as $BiFeO_3$ and metallic Bi (shown in the supporting information), as it can be expected from the synthesis reaction conditions and further purification processes made afterwards.

At first glance the spectra of our samples resemble that of α-Bi_2O_3 and β-Bi_2O_3, see Fig. 3 (b). However, a closer inspection reveals noticeable differences. The spectral shape of our samples basically consists on a main absorption peak (A) located at $\sim$ 13452 eV, a slight shoulder-like structure just below the main peak (A2, $\sim$13440 eV) and a single oscillation after the main peak. This directly suggests that the local order around Bi is short-range like that found in amorphous materials [20] and in metal ions in aqueous solution [29,38,39]. The spectral profile of both bismuth oxides, on the other hand, is richer. As can be seen in Fig. 3 (b) the spectra of α-Bi_2O_3 and β-Bi_2O_3 present a more evident shoulder-like structure just below the edge (A1, $\sim$ 13428 eV). In addition, the β-Bi_2O_3 compound shows a hump at E $\sim$ 13465 eV (B) followed by

Fig. 4 Comparison between the experimental Bi L_3-edge XANES of metallic Bi (blue, ○) and BiFeO$_3$ (black, ·) and the computations performed by using the DH ECP and ovf = 1%.
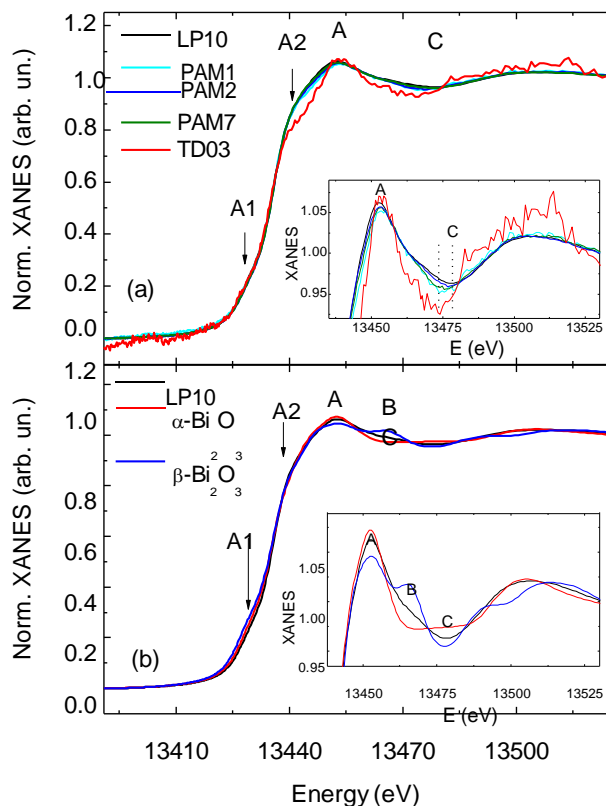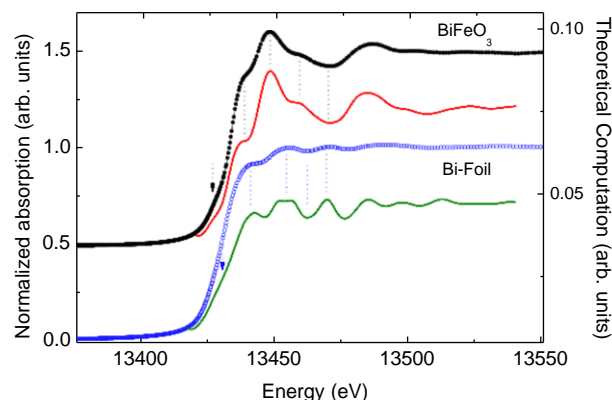

Fig. 3 (a) Comparison of the experimental Bi L_3-edge XANES spectra of all the bismuth-doped iron oxide nanoparticles. (b) Comparison of the experimental Bi L_3-edge XANES spectra of the LP10 sample and the α-Bi$_2$O$_3$ and β-Bi$_2$O$_3$ references.

a negative feature at higher energies (C) and the spectrum of α-Bi$_2$O$_3$ presents a wide plateau at the energy region right after A. Therefore, a more detailed study is needed to determine with higher precision if the local environment of Bi in the samples under study is just a distorted α-Bi$_2$O$_3$ or β-Bi$_2$O$_3$, a mixture of both oxides or a different Bi environment. To this aim we have performed an study including theoretical computations.

To compare the XANES experimental spectra to the results of *ab-initio* Bi L_3-edge computations, we need first to find the more appropriate choice of several computational parameters by using well known reference compounds [30,31]. Thus, initially we have computed the theoretical spectrum for metallic Bi and BiFeO$_3$. The results of the computations are reported in Fig. 4. The excellent agreement obtained allows us to fix several computational parameters as discussed in the experimental section. Hereafter all the calculations have been performed by using a 1% overlapping factor and the DH ECP potential.

Next, we have computed the XANES spectra for α-Bi$_2$O$_3$ and β-Bi$_2$O$_3$ polymorphs [40]. Computations have been done for different sizes: starting from the smallest Bi-O coordination polyhedron, corresponding to the photoabsorbing Bi and its first oxygen coordination shell, and adding progressively further coordination shells. The results of these calculations, shown in Fig. 5, indicate that a good reproduction of the experimental spectra requires a cluster including, at least, two coordination shells. In this way the relative energy separation of the spectral features is accounted for by the calculations, especially regarding the high energy resonances C (in α-Bi$_2$O$_3$) and D (β-Bi$_2$O$_3$). In other words, the inclusion of Bi-Bi coordination is mandatory to account for the experimental spectra.

These computations are also compared to the spectra of the
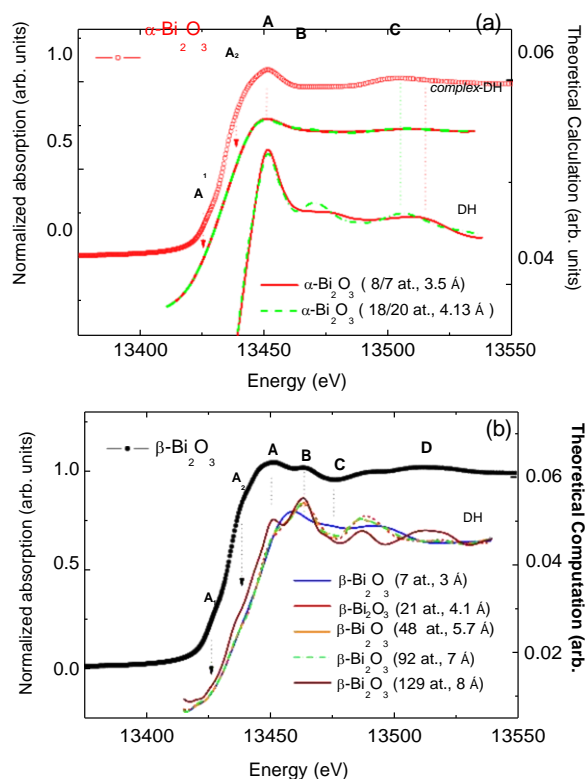
samples under study. As discussed above, the
region at ~

Fig. 5 (a) Comparison between the experimental Bi L_3-edge XANES of α-Bi$_2$O$_3$ (red, $\circ$) and the theoretical calculations performed by using the complex DH ECP and by progressively increasing the cluster size (see text for details). In order to get an enhanced view of the differences the result of the computations obtained by using the real DH are also shown. (b) Same as above, using only the real DH computations, in the case of β-Bi$_2$O$_3$ (black, $\cdot$).

13465 eV in the XANES spectra of our samples cannot be accounted for in terms of the presence of α-Bi$_2$O$_3$ or β-Bi$_2$O$_3$. To explain the XANES spectra of our samples one could suggest, in principle, that they contain a fraction of Bi atoms in a local arrangement similar to that of α-Bi$_2$O$_3$ and also a fraction of Bi atoms in a β-Bi$_2$O$_3$ fashion. If this was the case, the theoretical computations above would indicate that the local order around Bi includes not only oxygen but also the second shell, implying the existence of Bi-O-Bi coordination. However, as we will see below, no Bi-O-Bi coordination can be detected in the nanoparticles synthesized by laser pyrolysis or precipitation in aqueous media.

Finally, we have also computed the XANES spectra by considering that Bi substitutes Fe in several iron oxides: magnetite, maghemite and hematite. These theoretical results do not agree with the experimental spectra (see the Supporting Information). This indicates that Bi does not enter in the spinel structure, as suggested by the results at the Fe K edge.

3.4 Bi L_3-edge EXAFS - PAM and LP samples

The initial inspection of the EXAFS spectra verifies the absence of precursors, BiFeO$_3$ and segregated metallic Bi (see supplementary information). It also points out that the EXAFS spectral shape of our samples resembles to some extent that of α-Bi$_2$O$_3$ and β-Bi$_2$O$_3$, but it is notably less structured than that of either α-Bi$_2$O$_3$ or β-Bi$_2$O$_3$ (see Fig. 6). The profile of our samples consists of basically only one oscillation, whereas the Bi$_2$O$_3$ references show extra features reflecting the existence of additional scattering paths with significant contribution, i.e. longer range order. Therefore, the simpler profile of our samples can be addressed to the short-range character of the structural order around Bi. Fig. 6 also shows the EXAFS spectrum of a commercial Bi(OH)$_3$ reference. In the case of Bi(OH)$_3$ the simple profile of its EXAFS indicates short-range character of the structural order around Bi, similarly to LP10 and PAM7. It is worth to mention at this point that no detailed structural information has been reported for Bi(OH)$_3$, which is not a stable and well-defined compound. The lack of detailed crystallographic information (space group, lattice parameters, atomic positions, etc) prevents from performing any precise analysis of its EXAFS signal.

The short-range character of the structural order around Bi in the LP and PAM samples is also inferred from the comparison of the Fourier transforms (FT). As it can be seen in the right panel of Fig. 6 all the compounds show a main peak at ~ 1.6 Å corresponding to a first coordination shell made of oxygen atoms, but our samples have only a very small bump at ~ 3.2 Å, whereas the Bi$_2$O$_3$ references show a double peak due to Bi neighbors.

The analysis of the first peak of the FT shows that in the case of β-Bi$_2$O$_3$ the Bi-O bond distance is smaller (~ 0.06
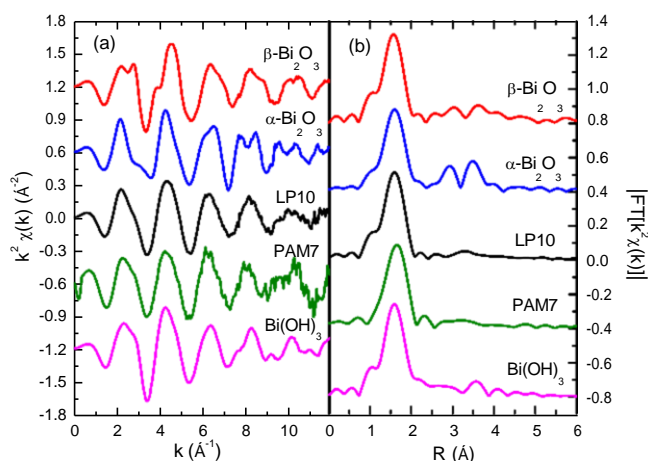
Fig. 6 (left panel) Comparison of the experimental Bi L$_3$-edge EXAFS spectra of the representative LP10 and PAM7 samples and the reference compounds α-Bi$_2$O$_3$, β-Bi$_2$O$_3$ and Bi(OH)$_3$. (right panel) Corresponding FT's. The spectra have been vertically shifted for the sake of clarity.
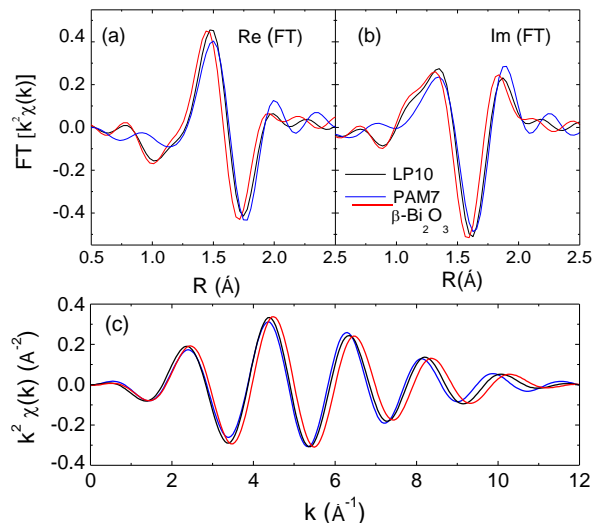

Fig. 7 Detail (0.5 Å - 2.5 Å range) of the real (a) and imaginary (b) parts of the Fourier transform corresponding to the Bi L$_3$-edge EXAFS of the LP10 (black), PAM7 (blue) and β-Bi$_2$O$_3$ (red) samples. (c) Fourier back-transform showing the shift in the contribution corresponding to the first peak.
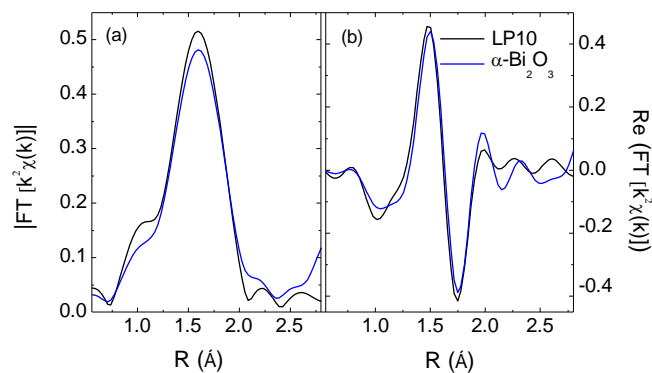
Fig. 8 Comparison of the modulus (a) and real part (b) of the Fourier transform obtained from the Bi L$_3$-edge EXAFS spectra of the LP10 (black) and the α-Bi$_2$O$_3$ (blue) samples.

Å) than in our samples (Fig. 7). As for the α-Bi$_2$O$_3$ case, although the Bi-O distance matches with that of our samples, the profile of the FT corresponding to the first shell is slightly different for α-Bi$_2$O$_3$ and LP10. And this profile changes from one sample to another. As it can be seen in the real part of the FT (Fig. 8), the region around R $\sim$ 1.9-2.4 Å does not match for both samples. Since the profile at the region 1-2.5 Å is determined by the details of the first coordination shell (number of atoms and distance), it can be concluded that in our samples the oxygen atoms in the first shell around Bi are arranged in a slightly different way than those in α-Bi$_2$O$_3$. A more quantitative comparison of the two environments has been included in the supplementary information. Similarly, the comparison to Bi(OH)$_3$ shows that the environments around Bi are very close for both Bi(OH)$_3$ and LP10. Still, the profile of the first peak of LP10 is slightly different to that of Bi(OH)$_3$.

More importantly, the analysis of the second shell does not show evidence of a Bi-Bi (neither of Bi-Fe) scattering path. The almost unnoticeable hump at $\sim$ 3.2 Å does not show the double peak profile one would expect for a Bi scatterer. Moreover, its relative amplitude does not grow with increasing k-weight as one can expect for a shell containing atoms with larger atomic number than oxygen. This is displayed in Fig. 9, where the FT spectra are plotted for different k-weights and normalized to the intensity of the first peak. According to this comparison the feature at $\sim$ 3.2 Å is, most likely, due to scattering from light atoms, such as O or H. The same conclusion is drawn from a Fourier back-transform analysis of this feature (in the supplementary information).

The results of the combined XANES and EXAFS analysis indicate that, in the case of the samples synthesized by laser pyrolysis or precipitation in aqueous media, the order around Bi is short-range and extends only to one coordination shell made of oxygen atoms. Moreover, the geometry of this first
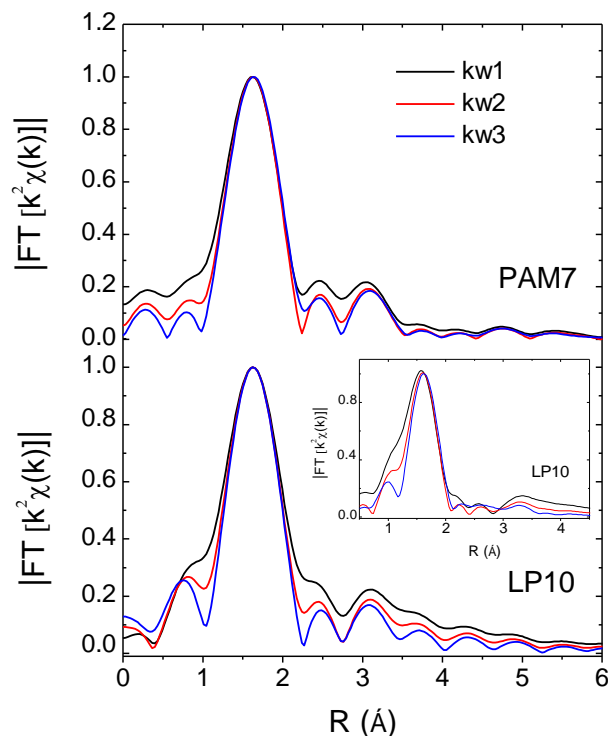
Fig. 9 Bi L3-edge FT (modulus, 2.5-8.5 Åk-range) plotted for different k-weights and rescaled so that the first shell has the same amplitude with all three k-weights. Inset: same comparison for a k-range from 2.0 to 10.0 Å.

shell cannot be accurately associated to that of α-Bi_2O_3 or β-Bi_2O_3 compounds. As for the analysis of the second shell, the almost unnoticeable hump at ~ 3.2 Å does not show evidence of a Bi-Bi (neither of Bi-Fe) scattering path. Not having a Bi-Bi scattering path, i.e. a Bi-O-Bi coordination, one can hardly say that the Bi is in a Bi_2O_3 crystalline structure, even disordered. Besides, certainly, a disordered α-Bi_2O_3 would give rise to a wider and less intense peak in the corresponding Fourier transforms but not to an almost complete extinction of the peak. Therefore, the formation of a defined Bi_2O_3 phase is discarded. Similarly, the hypothesis of Bi embedded in the Fe oxide structure can be undoubtedly discarded since in that case a clear second coordination shell should be seen.

From the above results one cannot rule out the hypothesis of having an entirely amorphous Bi oxide (i.e. BiO_x, where the structure and even the atomic proportion are not defined and no Bi-O-Bi coordination is mandatory at ~ 3-4 Å). However, taking into account the close resemblance of the EXAFS signals of LP10 and PAM7 to that of the bismuth hydroxide commercial reference, the k-weight dependence of our FTs, the small Bi concentration and the presence of hydrogen in the synthesis procedure , these results suggest that Bi may be in a Bi-hydroxide-like form where the formation of Bi-O-Bi bridges gets prevented by the non-bridging hydroxyl groups rather than in small, amorphous Bi oxide clusters. This would explain that Bi_2O_3 seeds are not formed avoiding the formation of a continuous layer and a well defined core-shell interface. Moreover, the presence of OH groups has been confirmed by TGA measurements (in the supplementary information).

Therefore, our results agree with bismuth being in a distorted octahedral, oxygen-based, local environment forming $[BiO_{6-x}(OH)_x]$ units (or similar) and being bonded through hydroxyl groups or adsorbed by van der Waals forces to the surface of the nanoparticle. The capping around the spinel nanoparticle consists, therefore, of isolated units bonded through intermolecular forces to the surface of the nanoparticle instead of a well formed Bi_2O_3 shell bounded to the core by Bi-O-Fe bridging bonds (intramolecular forces). This has strong implications for the stability and biofunctionality of this hybrid structure, which may depart from that expected for magnetite/bismuth oxide core /shell structures. Thus, the (OH) groups in the $[BiO_{6-x}(OH)_x]$ unit can interact with other compounds by attaching or exchanging new ligands and giving rise to further surface functionalization.

3.5 Bi L$_3$-edge XANES and EXAFS- TD03 sample

Regarding the TD03 sample, the profile of the FT of the EXAFS signal shows the presence of a second coordination shell in addition to the first oxygen shell, indicating longer range order around Bi (Fig. 10). For this sample, the amount of

bismuth is smaller (0.3%) than for the other samples. Consequently, the XAS signal is very small and with a poor signal-to-noise ratio and so doubts may be cast on any precise conclusion drawn form this spectrum. However, even though an accurate analysis cannot be done for this sample, our data clearly indicate that the thermal decomposition method gives rise to Bi local environments different from those obtained by laser pyrolysis or precipitation in aqueous media.

The analysis of the feature at ~ 3 Å discards a Bi-Bi origin since it should give rise to a double peak in the FT and to a double hump profile in the filtered EXAFS oscillations. On the other hand, the comparison of the filtered EXAFS corresponding to the second peak with the FEFF simulated Bi-O and Bi-Fe EXAFS contributions suggests that it is mainly made of oxygen atoms (or any other light atoms). Nevertheless, an additional contribution from Fe neighbors cannot be discarded. In fact, this FT resembles, to some extent, that found at the Fe K edge (see middle panel Fig. 2). The FT corresponding to the Bi L_3 edge can be roughly accounted for with a first shell of oxygen atoms at 2.09 Å, and a second shell of oxygen and iron atoms at 3.49 Å, which corresponds to a 0.2 Å expanded tetrahedral Fe site in Fe_3O_4. The environment around Bi in $BiFeO_3$ has also been tested but it has been excluded since its second shell is at a much smaller distance. In the case of the samples made by thermal decomposition, the synthesis temperature, $\sim$ 300 °C, is higher than for the other two methods. This could favor that the Bi atoms bond strongly to the iron oxide. Moreover, the oleic acid among the nanoparticles has a high interaction with these nanoparticles.[41] This could also help to keep the Bi atoms strongly bonded to the surface of the nanoparticle and in a more ordered environment. In this respect, it cannot be discarded the idea of Bi atoms being also bonded to the oleic acid, $(CH_3(CH_2)_7CH = CH(CH_2)_7COOH)$. However, these bonds alone could hardy explain the second peak at the FT since, although a precise value for the number of atoms in the second shell cannot be given at this point, the high amplitude of this peak indicates a high coordination number.

4 Conclusions

The structural characterization of Bi-doped iron oxide nanoparticles grown by three different methods has been carried out by X-ray absorption spectroscopy recorded at the K edge of Fe and the L_3 edge of Bi. Our results discard the formation of Bi metal (Bi-Bi direct bonds). In addition, in the case of particles grown by laser pyrolysis or precipitation in aqueous media, they show that the Bi atoms neither enter in the iron oxide spinel lattice nor form any other Bi oxide. The bismuth atoms are in an oxygen-based local environment whose order extends only to one coordination shell. Contrary to expectations, the results discard the possibility of having a well defined core-shell (magnetite-bismuth oxide) structure.
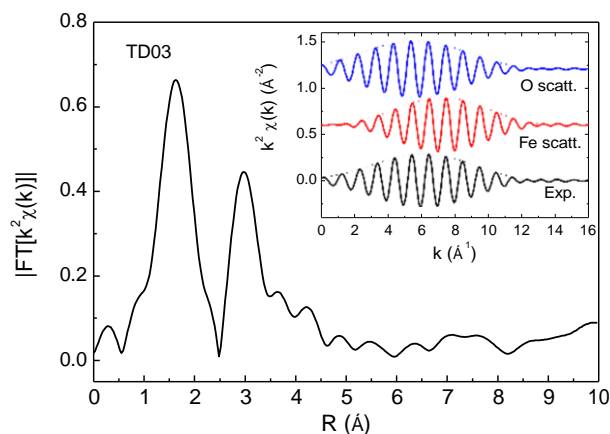

Fig. 10 Modulus of the FT of the experimental Bi L_3-edge EXAFS spectra of the TD03 sample (inset) Real part of the second shell Fourier filtered EXAFS oscillaltions.

Our data agree with a hybrid structure made of an iron oxide core and a capping consisting on isolated $[BiO_{6-x}(OH)_x]$ (or similar) units bonded through chemisorption with hydroxyl groups to the surface of the nanoparticle. On the other hand, in the sample grown by thermal decomposition, the longer-range ordered environment suggests that the Bi atoms are embedded in the spinel lattice, either at the Fe tetrahedral site or at the surface of the nanoparticle but more strongly bonded to the iron oxide. The presented results provide valuable information to better understand the physicochemical properties of Bi-doped magnetite nanoparticles as well as their possibilities for further functionalization and application as double contrast agents for imaging.

5 Acknowledgements

References

1 J. Cheon and J.-H. Lee, *Accounts of Chemical Research*, 2008, **41**, 1630.

2 J. H. Lee, J. W. Kim and J. Cheon, *Mol Cells*, 2013, **35**, 274.

3 S. Laurent, D. Forge, M. Port, A. Roch, C. Robic, L. V. Elst and R. N. Muller, *Chem. Rev.*, 2008, **108**, 2064.

4 A. G. Roca, R. Costo, A. F. Rebolledo, S. Veintemillas-Verdaguer, P. Tartaj, T. González-Carreño, M. P. Morales and C. J. Serna, *J. Phys., D: Appl. Phys.*, 2009, **42**, 224002.

5 P. Tartaj, M. P. Morales, T. González-Carreño, S. Veintemillas-Verdaguer and C. J. Serna, *Adv. Mater.*, 2011, **23**, 5243.

6 C. Corot, P. Robert, J.-M. Ide and M. Port, *Advanced Drug Delivery reviews*, 2006, **58**, 1471.

7 J. H. Lee, Y. M. Huh, Y. W. Jun, J. W. Seo, J. T. Jang, H. T. Song, S. Kim, E. J. Cho, H. G. Yoon, J. S. Suh and J. Cheon, *Nat. Med.*, 2007, **13**, 95.

8 L. Sun, Y. Zang, M. Sun, H. Wang, X.Zhu, S. Xu, Q. Yang, Y. Liu and Y. S. and, *J. Colloid Interface Sci.*, 2010, **350**, 90.

9 N. Lee, S. H. Choi and T. Hyeon, *Adv Mater*, 2013, **25**, 2641.

10 G. G. Briand and N. B. Burford, *Chem. Rev.*, 1999, **99**, 2601.

11 W. A. Kalender, *Physics in medicine and biology*, 2006, **51**, R29–43.

12 X. Pan, J. Siewerdsen, P. J. L. Riviere and W. A. Kalender, *Medical physics*, 2008, **35**, 3728.

13 O. Rabin, J. M. Perez, J. Grimm, G. Wojtkiewicz and R. Weissleder, *Nat Mater*, 2006, **5**, 118–122.

14 M. Andrés-Vergés, M. P. Morales, S. Veintemillas-Verdaguer, F. J. Palomares and C. J. Serna, *Chem. Mater.*, 2012, **24**, 319.

15 M. Andrés-Vergés, R. Costo, A. G. Roca, J. F. M. G. F. Goya, C. J. Serna and M. P. Morales, *J Phys D Appl Phys*, 2008, **41**, 134003.

16 S. Veintemillas-Verdaguer, M. P. Morales and C. J. Serna, *Mater Lett*, 1998, **35**, 227.

17 M. C. Bautista, O. Bomati-Miguel, M. P. Morales, C. J. Serna and S. Veintemillas-Verdaguer, *Journal of Magnetism and Magnetic Materials*, 2005, **293**, 20.

18 A. G. Roca, S. Veintemillas-Verdaguer, M. Port, C. Robic, C. J. Serna and M. P. Morales, *Journal of Physical Chemistry B*, 2009, **113**, 7033.

19 A. D. Cicco, G. Aquilanti, M. Minicucci, E. Principi, N. Novello, A. Cognigni and L. Olivi, *J. Phys.: Conf. Ser.*, 2009, **190**, 012043.

20 D. E. Sayers and B. Bunker, in *X-Ray Absorption: Principles, Applications, Techniques of EXAFS, SEXAFS, and XANES*, ed. D. C. Koningsberger and R. Prins, Wiley: New York, 1988, ch. 6.

21 M. Newville, *J. Synchrotron Rad.*, 2001, **8**, 322.

22 B. Ravel and M. Newville, *J. Synchrotron Rad.*, 2005, **12**, 537.

23 C. R. Natoli, D. Misemer, S. Doniach and F. Kutzler, *Phys. Rev. A*, 1980, **22**, 1104.

24 M. Benfatto and S. D. Longa, *J. Synchrotron Rad.*, 2001, **8**, 1087.

25 J. Chaboy, H. Maruyama and N. Kawamura, *J. Phys.: Condens. Matter*, 2007, **19**, 216214.

26 J. Chaboy, N. Nakajima and Y. Tezuka, *J. Phys.: Condens. Matter*, 2007, **19**, 266206.

27 C. Guglieri and J. Chaboy, *J. Phys. Chem. C*, 2010, **114**, 19629.

28 C. Guglieri, E. Céspedes, C. Prieto and J. Chaboy, *J. Phys.: Condens. Matter*, 2011, **23**, 206006.

29 S. Díaz-Moreno, A. Muñoz-Páez and J. Chaboy, *J. Phys. Chem. A*, 2000, **104**, 1278.

30 J. Chaboy and S. Quartieri, *Phys. Rev. B*, 1995, **52**, 6349.

31 J. Chaboy, *J. Synchr. Rad.*, 2009, **16**, 533.

32 J. Chaboy, A. Muñoz-Páez, F. Carrera, P. Merkling and E. Sánchez-Marcos, *Phys. Rev. B*, 2005, **71**, 134208.

33 M. O. Krause and J. Oliver, *J. Phys. Chem. Ref. Data*, 1979, **8**, 329.

34 C. Piquer, M. A. Laguna-Marco, A. G. Roca, R. Boada, C. Guglieri and J. Chaboy, *J. Phys. Chem. C*, 2014, **118**, 1332–1346.

35 *Introduction to XAFS: A Practical Guide to X-ray Absorption Fine Structure Spectroscopy*, ed. G. Bunker, Cambridge University Press, U.K., 2010.

36 P. Glatzel, G. Smolentsev and G. Bunker, *J. Phys.: Conf. Ser.*, 2009, **190**, 012046.

37 F. Farges, *Phys. Chem. Miner.*, 2009, **36**, 463.

38 A. Zitolo, V. Migliorati, G. Aquilanti and P. D'Angelo, *Chem. Phys. Lett.*, 2014, **591**, 32 – 36.

39 J. Chaboy and S. Díaz-Moreno, *J. Phys. Chem. A*, 2011, **115**, 2345–2349.

40 H. A. Harwig, *Z. Anorg. Allgem. Chem.*, 1978, **444**, 151.

41 A. G. Roca, M. P. Morales, K. O'Grady and C. J. Serna, *Nanotechnology*, 2006, **17**, 2783.